

REPORT DOCUMENTATION PAGE

*Form Approved
OMB No. 0704-0188*

Public reporting burden for this collection of information is estimated to average 1 hour per response, including the time for reviewing instructions, searching existing data sources, gathering and maintaining the data needed, and completing and reviewing this collection of information. Send comments regarding this burden estimate or any other aspect of this collection of information, including suggestions for reducing this burden to Department of Defense, Washington Headquarters Services, Directorate for Information Operations and Reports (0704-0188), 1215 Jefferson Davis Highway, Suite 1204, Arlington, VA 22202-4302. Respondents should be aware that notwithstanding any other provision of law, no person shall be subject to any penalty for failing to comply with a collection of information if it does not display a currently valid OMB control number. PLEASE DO NOT RETURN YOUR FORM TO THE ABOVE ADDRESS.

1. REPORT DATE (DD-MM-YYYY) 09-09-2010		2. REPORT TYPE Journal Article		3. DATES COVERED (From - To)	
4. TITLE AND SUBTITLE Ionizing Shocks in Argon. Part 2: Transient and Multi-Dimensional Effects (Preprint)		5a. CONTRACT NUMBER			
		5b. GRANT NUMBER			
		5c. PROGRAM ELEMENT NUMBER			
6. AUTHOR(S) M.G. Kapper (von Karman Institute); J.-L. Cambier (AFRL/RZSS)		5d. PROJECT NUMBER			
		5f. WORK UNIT NUMBER 23040256			
7. PERFORMING ORGANIZATION NAME(S) AND ADDRESS(ES) Air Force Research Laboratory (AFMC) AFRL/RZSS 1 Ara Road Edwards AFB CA 93524-7013		8. PERFORMING ORGANIZATION REPORT NUMBER AFRL-RZ-ED-JA-2010-383			
9. SPONSORING / MONITORING AGENCY NAME(S) AND ADDRESS(ES) Air Force Research Laboratory (AFMC) AFRL/RZS 5 Pollux Drive Edwards AFB CA 93524-7048		10. SPONSOR/MONITOR'S ACRONYM(S)			
		11. SPONSOR/MONITOR'S NUMBER(S) AFRL-RZ-ED-JA-2010-383			
12. DISTRIBUTION / AVAILABILITY STATEMENT Approved for public release; distribution unlimited (PA #10441).					
13. SUPPLEMENTARY NOTES For publication in the Journal of Applied Physics.					
14. ABSTRACT We extend the computations of ionizing shocks in argon to unsteady and multi-dimensional, using a collisional-radiative model and a single-fluid, two-temperature formulation of the conservation equations, described in part 1 of this article. We show that the fluctuations of the shock structure observed in shock-tube experiments can be reproduced by the numerical simulations, and explained on the basis of the coupling of the non-linear kinetics of the collisional-radiative model with wave propagation within the induction zone. The mechanism is analogous to instabilities of detonation waves and also produces a cellular structure commonly observed in gaseous detonations. We suggest that the detailed simulations of such unsteady phenomena can yield further information for the validation of non-equilibrium kinetics.					
15. SUBJECT TERMS					
16. SECURITY CLASSIFICATION OF:			17. LIMITATION OF ABSTRACT SAR	18. NUMBER OF PAGES 11	19a. NAME OF RESPONSIBLE PERSON Dr. Jean-Luc Cambier
a. REPORT Unclassified	b. ABSTRACT Unclassified	c. THIS PAGE Unclassified			19b. TELEPHONE NUMBER (include area code) N/A

Ionizing Shocks in Argon. Part 2: Transient and Multi-Dimensional Effects (Preprint)

M. G. Kapper^{1,2} and J.-L. Cambier¹

¹⁾Air Force Research Laboratory

10 E. Saturn Blvd.

Edwards AFB, CA 93524, USA

²⁾von Karman Institute, Brussels, Belgium.

(Dated: 10 September 2010)

We extend the computations of ionizing shocks in argon to unsteady and multi-dimensional, using a collisional-radiative model and a single-fluid, two-temperature formulation of the conservation equations, described in part 1 of this article. We show that the fluctuations of the shock structure observed in shock-tube experiments can be reproduced by the numerical simulations, and explained on the basis of the coupling of the non-linear kinetics of the collisional-radiative model with wave propagation within the induction zone. The mechanism is analogous to instabilities of detonation waves and also produces a cellular structure commonly observed in gaseous detonations. We suggest that the detailed simulations of such unsteady phenomena can yield further information for the validation of non-equilibrium kinetics.

Keywords: Non-Equilibrium Collisional-Radiative Plasma Shocks

I. INTRODUCTION

In Part 1 of this article we studied the steady-state, one-dimensional solutions of an ionizing shock in Argon using a detailed collisional-radiative model. In this second part, we focus on the unsteady and two-dimensional features of the problem. While there have been numerous studies of ionizing shock propagation in noble gases, it was not until the shock tube experiments conducted at the Institute for Aerospace Studies, University of Toronto (UTIAS),¹ that it was shown that under certain conditions, a definite dynamical behavior could be associated with a strong ionizing shock in argon. It was discovered that the translational shock front propagating in pure argon “develops sinusoidal instabilities which affect the entire shock structure including the ionization relaxation region, the electron cascade front, and the final quasi-equilibrium state.” Deviations from ideal, one-dimensional shock solutions are frequently found in practice, due to finite-size effects in experimental devices. Thus, shock curvature and boundary-layer effects in ionizing shocks can be expected. For example, Bristow² postulated the presence of “weak forward moving oblique shocks” while Brimelow³ showed that in pure argon, premature ionization occurred close to the wall (1–2mm), which can be easily explained from the frictional heating in the developing boundary layer. However, Bristow also noticed a multiply curved shock front with what appeared to be transverse waves, an effect he conjectured could be caused by amplification of acoustic perturbations through thermal non-equilibrium effects. Buchanan performed time-resolved interferometry as well as Schlieren imagery and noticed transverse-moving and colliding shocks. Thus, he obtained images with cross-hatching features which resembled the pattern left by a multi-headed gas-detonation wave on a soot-covered wall. He also computed the cell size from the number of

half-sine waves that were present across the translational front. Houwing *et al.*⁴ carried out shock-tube experiments under similar conditions to the UTIAS cases and observed similar instabilities, albeit not as a dramatic. However their shock tube had a much smaller cross section with a diameter of 5cm, compared to the 10x18 cm shock tube at UTIAS. The presence of impurities can also affect the nature of the relaxation region. Bristow showed that adding a small amount (0.4% partial pressure) of H_2 was sufficient to make the shock planar. Therefore, the absence of instabilities in some experimental results may very well be a result of length scales and experimental conditions, notably gas purity.

Drawing from the summarizing work of Glass & Liu¹, Cambier⁵ studied the transient effects of such shocks in a series of numerical experiments, verifying the concept of a “resonant cavity” phenomena proposed by Bristow. Modeling the same conditions as the UTIAS experiments he was able to obtain self-sustaining oscillations of the shock front that were similar to the galloping instabilities of detonation waves. It was shown that the instabilities were sensitive to the collisional-radiative kinetics and that the instabilities would be damped if the excitation and ionization cross sections fell outside a given range. He also verified the effect of molecular impurities in the dampening of instabilities. However, that work was performed only in one dimension and with a very simplified collisional-radiative model; the relationship with the cell pattern experimentally observed could only be conjectured, although Cambier was able to predict the ionization cell size to a satisfactory degree. We extend here this study to two dimensions in order to clearly demonstrate the mechanism responsible for instabilities in ionizing shocks in pure noble gases. Since instabilities were observed in both two and three dimensions, it is sufficient to perform these computations in (planar) 2D—extension to 3D unsteady calculations is contemplated for the near future.

II. GOVERNING EQUATIONS

A. Plasma thermodynamics

We describe the plasma as a neutral single-fluid, two-temperature flow. The individual electronic states of neutral argon are separately convected as different species, allowing a non-Boltzmann description of the Atomic State Distribution Function (ASDF). Charge neutrality is guaranteed by the small Debye length scale and the absence of applied electric fields, while a single fluid velocity is a consequence of the large effective frequency for collisional momentum exchange between the various plasma components, for the typical densities of interest here. Presently, we neglect viscous and species diffusion effects. In a finite-volume framework, the hyperbolic system of equations has the following form:

$$\frac{d}{dt} \int_V Q \, dV + \oint_A \hat{n} \cdot F \, dA = \int_{V(t)} \dot{\Omega} \, dV \quad (1)$$

where V is the volume of an elementary fluid "cell", A is the bounding area and \hat{n} its normal. Q is the vector of conserved variables, F is the flux and $\dot{\Omega}$ contains the source terms due to the kinetics of the collisional-radiative processes. The conserved variables and the normal flux can be written as:

$$Q = \begin{pmatrix} \rho_1 \\ \vdots \\ \rho_n \\ \rho u \\ \rho v \\ \rho w \\ E \\ \rho \hat{s}_e \end{pmatrix}, \quad F_n = \begin{pmatrix} \rho_1 v_n \\ \vdots \\ \rho_n v_n \\ \rho u v_n + n_x p \\ \rho v v_n + n_y p \\ \rho w v_n + n_z p \\ v_n H \\ \rho \hat{s}_e v_n \end{pmatrix}, \quad (2)$$

with

$$E = E_h + E_e + \frac{1}{2} \rho \vec{u}^2 \quad (3)$$

the total energy density of the plasma and $H = E + p$ the total enthalpy density and $p = p_h + p_e$ is the total gas pressure. We define $S_e = \rho \hat{s}_e$, with $\hat{s}_e = P_e / \rho^{\gamma_e}$ as an entropy-like variable, used instead of the thermal energy of the electron in order to maintain a strictly hyperbolic formulation⁶. This is necessary for accurate determination of the electron temperature across the shock discontinuity. Note also that we use the total mass density in the definition of S_e instead of ρ_e , to avoid singular values in the limit of vanishing ionization fraction. Total differentials of the conserved variables can be obtained (see Part 1):

$$dp(Q) = \sum_i \left(\frac{\partial p}{\partial Q_i} \right)_{Q_j} \quad (j \neq i)$$

i.e. the partial derivatives are evaluated for all other conserved variables being constant (see Appendix A). The derivatives of the pressure are thus obtained and using the notation $P_{q_i} = \frac{\partial p}{\partial q_i}$, we obtain the speed of sound:

$$a^2 = \sum \frac{\rho_s}{\rho} P_{\rho_s} + \left(\varepsilon + \frac{p}{\rho} - \frac{\vec{u}^2}{2} \right) P_E + \hat{s}_e P_{S_e} \quad (4)$$

The hyperbolic system of the Euler equations has the set of eigenvalues $v_n, v_n \pm a$ and Q and F can be decomposed according to the left and right eigenvectors (see A). Thus the Jacobian is:

$$A = \left(\frac{\partial F}{\partial Q} \right) = R \cdot \Lambda \cdot L \quad (5)$$

The term $\dot{\Omega}$ contains the source terms, both collisional and radiative, and is described in complete detail in article 1.

B. Numerical Scheme

The system is solved using the operator-splitting approach: at each time step the convective terms are solved independently of the source terms and the conserved variables are updated for each cell via

$$Q^{n+1} = Q^n + \Delta Q_{\text{CONV}} + \Delta Q_{\text{CR}} \quad (6)$$

Because of the short-time scales involved, the collisional-radiative source terms are updated implicitly,

$$\Delta Q_{\text{CR}} = \Delta t (I - J \Delta t)^{-1} \dot{\Omega}(Q^n) \quad (7)$$

requiring computation of the Jacobian, $J = \partial \dot{\Omega} / \partial Q$, and the use of a Gauss-Jordan elimination step. The convective terms are updated by the second-order Adams-Bashforth integration scheme, which uses the fluxes $F(Q)$ computed at a time-interpolated value of the conserved variables, using current and previous solutions:

$$\Delta Q_{\text{CONV}} = -\frac{\Delta t}{V} \sum_s \tilde{F}_{\hat{n}_s} \left(\frac{3}{2} Q^n - \frac{1}{2} Q^{n-1} \right) A_s \quad (8)$$

the summation being over all faces of a computational cell, with normal vectors \hat{n}_s directed outwards. An advantage of the Adams-Bashforth scheme is the fact that the fluxes need to be evaluated once, as opposed to a multi-step method like Runge-Kutta; this also reduces the overhead of message-passing in distributed-memory architectures.

The term \tilde{F} in Eq. 8 denotes the numerical flux which we compute using the HLLE Riemann solver⁷,

$$\tilde{F} = \frac{b^+ F_L - b^- F_R}{b^+ - b^-} + \frac{b^+ b^-}{b^+ - b^-} (Q_R - Q_L) \quad (9)$$

The upwind wave speeds b are given by

$$b^+ = \max(0, v_{n,R} + a_R, \tilde{v}_n + \tilde{a}) \quad (10)$$

$$b^- = \min(0, v_{n,L} - a_L, \tilde{v}_n - \tilde{a}) \quad (11)$$

where the tilde symbol ($\tilde{\cdot}$) is used to denote the Roe-average value at the cell interface. High-order spatial resolution is achieved via parabolic interpolation of the left and right states at the cell interfaces via

$$Q_L = \frac{1}{6}(2\bar{Q}_{j-1} + 5\bar{Q}_j - \bar{Q}_{j+1}) \quad (12)$$

making the scheme 3rd-order accurate⁸. We use the bar ($\bar{\cdot}$) symbol to differentiate cell-average quantities from point values. Strong nonlinear waves require limiting, which modifies the left and right states according to

$$Q_L \leftarrow \text{median}(Q_L, \bar{Q}_j, Q^{\text{MP}}) \quad (13)$$

with

$$Q^{\text{MP}} = \bar{Q}_j + \text{minmod}[\bar{Q}_{j+1} - \bar{Q}_j, \alpha(\bar{Q}_j - \bar{Q}_{j-1})] \quad (14)$$

being the monotonicity-preserving (MP) limit⁹. Here, we choose the parameter α to be 2. The right state is easily found from symmetry. Due to the non-linearity of the limiter, the reconstruction is performed on the characteristic variables, requiring a full diagonalization of the governing equations.

III. 1D RESULTS

A. Fluctuation Patterns

The CR model depends on the values of the cross-sections of elementary processes. Some of them are uncertain, in particular atom-atom inelastic collisions; thus, in article 1 the CR model was calibrated against experimental data for the steady-state case. In this section we examine the effect of unsteady coupling between the kinetics and transport, using the unsteady solver described above. Initial work on such unsteady effects verified the existence of oscillations in the form of longitudinal pulsations in the direction of the flow⁵. Building upon this work, similar numerical experiments are carried out here, albeit with a more detailed CR model and higher-order accuracy.

The conditions of the shock tube experiments were simulated numerically by impinging argon gas upon an ideally reflecting wall, thereby initiating a shock that propagates against the incoming flow as illustrated in Figure 1. Note that the free-stream conditions listed therein correspond to a shock with an initial strength of Mach 19. As the shock reflects from the wall, its Mach number decreases as the thermal energy is quickly converted to electronic energy in the form of bound excited states as well as free electrons, until a quasi-steady limit is reached. Thus, the freestream conditions provided in the figure are those used to reproduce the Mach 15.9 shock in the laboratory frame, corresponding to the first case of Table I of Part 1. The computational domain being fixed, a higher resolution can be obtained for choosing this reference frame with a lower propagation speed

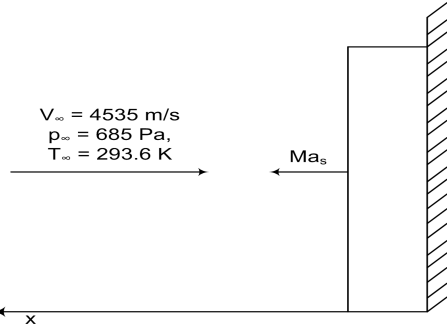


FIG. 1. Numerical setup for unsteady 1D shock tube simulations.

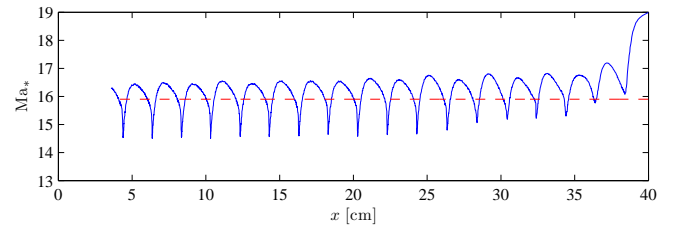


FIG. 2. Instantaneous Mach number as a function of distance from the wall located at 40 cm for Mach 15.9 case.

of the shock front, while avoiding the potential effects of a subsonic boundary condition. During the calculations, we can easily monitor local and global variables, such as the instantaneous shock Mach number in the laboratory frame and the "induction" length, i.e. the separation between the shock front and the avalanche region; the latter is identified by the location where the electron density has reached peak value.

The results in Figures 2 and 3 clearly show undamped, periodic fluctuations in both the shock Mach number as well as the induction length (in blue) compared to the experimental (averaged) value (dashed red line). These oscillations have a periodicity of approximately 32.5 μ sec and are characteristic of the experimental observations. As evident in the discontinuous shifts of the induction length, the oscillations do not vary smoothly, signaling a strong non-linear behavior. In fact, this behavior

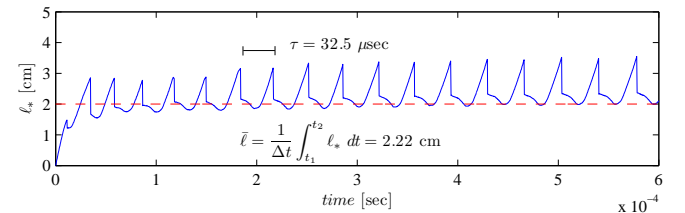


FIG. 3. Instantaneous induction length as a function of time for Mach 15.9 case. Dashed red line indicates the experimentally observed value of 2 cm. The fluctuation periodicity is 32.5 μ sec, with an induction length of 2.22 cm averaged over one period.

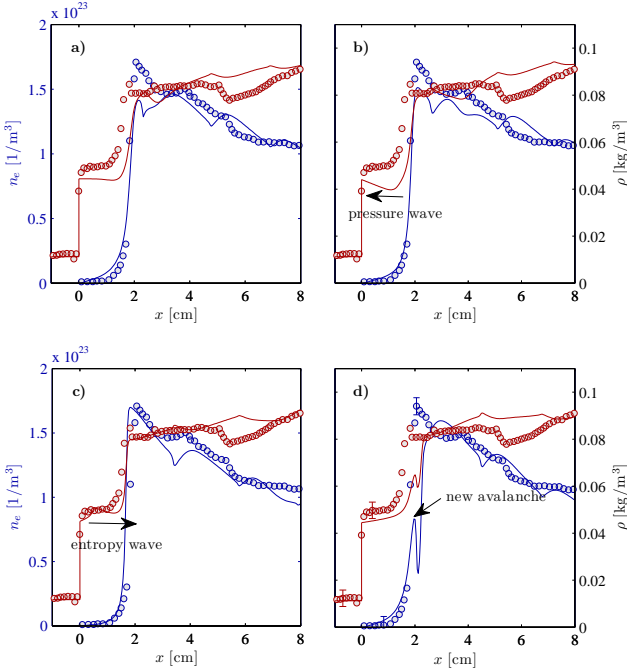


FIG. 4. Dynamic evolution of 1D ionizing shock structure: a) quasi-equilibrium state b) pressure wave initiated at electron avalanche travels towards compression shock c) after overtaking shock, pressure wave is reflected as an entropy wave due to strengthening of shock d) sensitivity of excitation and ionization rates to temperature jump across entropy wave results in earlier onset of electron avalanche. The process then repeats.

could be well approximated by the square-wave model for detonations¹⁰ in which the kinetics are assumed to be frozen below a certain threshold, but infinitely fast above it, reaching equilibrium instantaneously. This necessitates the introduction of an average induction length over a period,

$$\bar{\ell} = \frac{1}{\Delta t} \int_{t_1}^{t_2} \ell_* dt, \quad (15)$$

with ℓ_* being the instantaneous induction length. The computed value is shown in 3 and compares well with the experimental value (itself an approximation).

In regards to the discontinuous change in the induction length exhibited in this particular case, there is evidence that these anomalies have a physical origin. A sequence of characteristic profiles is shown in Figure 4. From top-down and left-right, the computed profiles of the mass density (red line) and electron density (blue line) are shown, compared to a snapshot of the experimental values (symbols). Disturbances of the total and electron densities are seen to propagate from the avalanche region towards the shock and reflected back. The perturbation in temperature is such that, given the highly non-linear kinetics within the induction zone (see article 1), the location of the avalanche can be significantly altered. As seen in Figure 4-d, a new "spot" where the ionization

avalanche occurs can be clearly identified. This will create in turn a new location for the peak ionization and a corresponding pressure wave (electron pressure) which couples back to the shock front, and the process is repeated.

The nature of this process can be better demonstrated with the space-time plots given in Figure 5. The plots clearly show pressure waves emerging from the electron avalanche, that travel in both directions. This can be considered the initiation of the fluctuation cycle. The forward-moving wave (left in the x-t diagram) overtakes the shock, thereby increasing its temperature and speed; the interaction also produces a rarefaction wave due to the acceleration of the shock which is too weak to notice on that figure. The resulting high temperature region generated behind the shock is separated from the previous post-shock region by a contact wave that can be seen as traveling away from the shock as it accelerates. Identification of the contact wave is trivially done by comparing the x-t diagrams for pressure and density. A more detailed reproduction of the (computed) x-t diagram is shown in Figure 6.

The temperature jump across the contact wave is crucial. Due to the exponential dependence on temperature, a relatively small jump can accelerate the kinetics and cause the electron avalanche to form much sooner than its quasi-equilibrium position. If the non-linear process leading to the avalanche is sufficiently fast and sensitive, this shift in the avalanche region can be discontinuous, as seen in Figure 4, i.e. the electron density profile in the induction region is non-monotonous—alternatively, if we consider the location of peak ionization, we see a bifurcation. This process is entirely analogous to the mechanism for detonation wave fluctuations proposed by Alpert and Toong¹¹, and was reproduced in numerical simulations of gaseous detonations (e.g. see¹²).

This explanation of the fluctuation mechanism can be confirmed by a simple estimation of the periodicity of the oscillations from basic wave theory. In⁵ it was shown that the period can be approximated by

$$\tau = \bar{\ell} \left(\frac{1}{a_2 - u_2} + \frac{1}{u_2} \right), \quad (16)$$

assuming that the pressure wave travels towards the shock with the nonlinear wave speed $a_2 - u_2$, while the entropy wave reflected from the shock travels with velocity u_2 , where the subscript 2 denotes the post-shock state. With $u_2 = 1284\text{m/s}$ and $a_2 = 2852\text{m/s}$ taken as the post-shock fluid and sound speeds respectively, the estimated periodicity is $31.4\mu\text{sec}$ which agrees well with the observed value of $32.5\mu\text{sec}$ (cf. Figure 3).

B. Sensitivity to cross sections

We examined the calibration of some key cross-sections in article 1 using the induction length in the steady-state

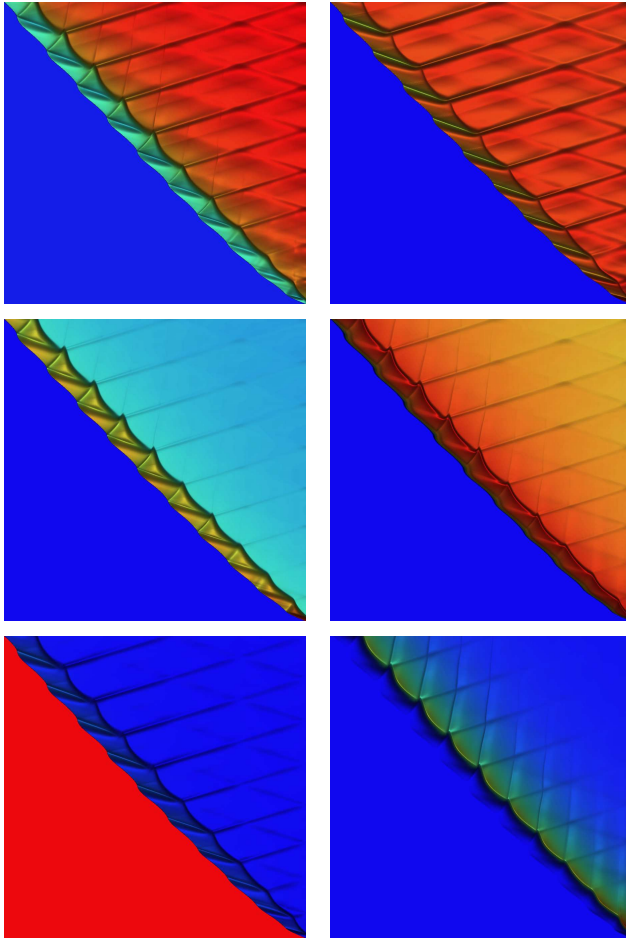


FIG. 5. x - t diagrams for 1D Ma 14.7 case. From top row: total density (ρ) on the left, total pressure (p) on the right; heavy-particle temperature (T_h , left), electron temperature (T_e , right); on the last row, velocity (V_x , left) and ionization fraction (α , right). Gradients are enhanced through shading effects. Colormap: min max

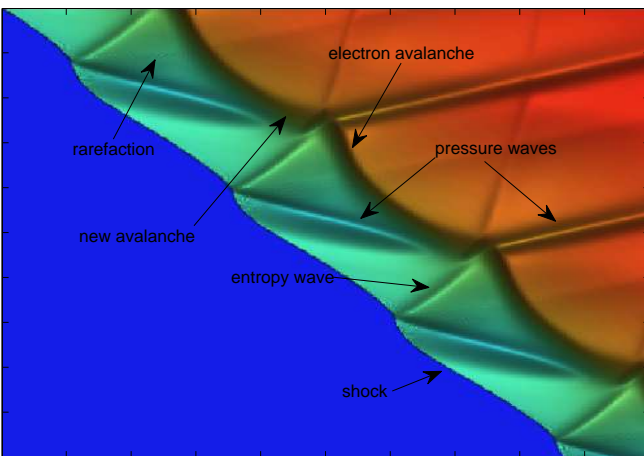


FIG. 6. x - t diagrams for 1D Ma 14.7 case - total density (detail).

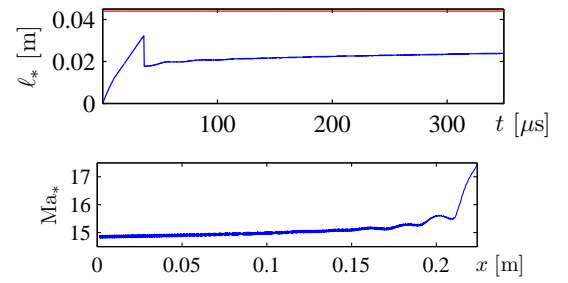


FIG. 7. Sensitivity of induction length and shock Mach number to cross sections for 1D unsteady calculations; using Drawin's excitation cross sections.

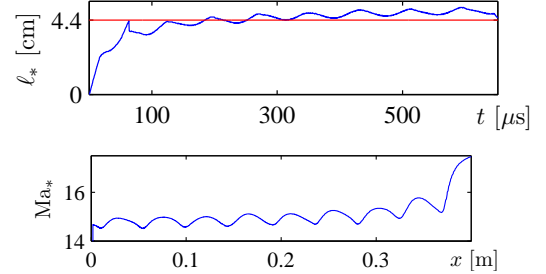


FIG. 8. Sensitivity of induction length and shock Mach number to cross sections for 1D unsteady calculations; reducing the atom impact excitation cross-sections by factor of 10

case, but it may also be possible to use the unsteady features to place bounds on these cross-sections. For that, knowing the effect of the cross sections on the dynamics of the oscillations is crucial. While an analytical approach to stability analysis is not pursued here, semi-empirical considerations can serve as a valuable precursor to such studies.

As a first test, the Mach 14.7 case was run using the atom-atom impact excitation cross sections as computed from Drawin's formula, Eq. (17), without modification.

$$\sigma_{ij}^a(\varepsilon) = 4\pi a_o^2 \left(\frac{I_H}{\varepsilon_{ij}} \right)^2 \frac{m_{Ar}}{m_H} \xi^2 f_{ij} \times \frac{2m_e}{m_{Ar} + m_e} \frac{\varepsilon/I_i - 1}{\left(1 + \frac{2m_e}{m_{Ar} + m_e} (\varepsilon/I_i - 1) \right)^2} \quad (17)$$

where I_H is the ionization potential of the hydrogen atom and $\xi = 6$ is the number of optical electrons of argon. As a reminder, the resulting rates are more than a factor of 10 greater than those used to obtain the solutions with the experimentally-observed induction length. Comparing the results shown in Figures 7 and 8 indicate that the large atom-impact excitation cross sections obtained from Drawin's formula essentially halves the induction length compared to the observed value (8). Furthermore, the influence on the oscillations is quite pronounced, resulting in significant damping to the point that the oscillations can no longer be sustained. This can be explained

as follows: as the pressure wave emanating from the electron avalanche overtakes the compression shock, the heavy particle temperature T_h increases. This in turn increases the atom-impact excitation, the rate having a sensitive exponential dependence on T_h . The atom-impact inelastic processes acts as an energy sink, effectively absorbing energy from the pressure wave and dampening the oscillations.

In a separate test, the electron-atom impact excitation cross sections were reduced by a factor of 10. In this case the atom impact excitation cross sections were also modified so that the induction length was close to 4.4 cm as seen in Figure 8. While the oscillations still persisted in this case, the discontinuous change in the induction length (cf. Figure 2) had disappeared. Instead, the oscillations vary smoothly over the entire period of the fluctuation. This key observation can be explained from the association of the discontinuous shift with a highly sensitive non-linear coupling with exponential temperature dependence of the rate equations; this dependence can be well-approximated by the square-wave model for detonation phenomena as previously noted. As the electron-impact cross sections are decreased, the strength of the non-linear coupling diminishes and other processes such as thermalization become relatively stronger. This slows the rate of onset of the electron avalanche and gives the fluid more time to “react” to the kinetics.

IV. 2D RESULTS

A. Test Setup

With a general understanding of the oscillation mechanism and the resulting wave pattern obtained from the unsteady 1D simulations, we can now extend the simulations and theory to a two-dimensional problem. With another dimension, the observed oscillations are no longer confined to the longitudinal direction, leading to the possibility of transverse waves. While this opens the door to more complex wave interactions and structures, a systematic approach that extends the ideas of the previous section in a straight-forward manner is taken here.

The 2D simulations were conducted on the domain $0 \leq x \leq 54$ cm, $0 \leq y \leq 18$ cm, with a depth of 10 cm¹³. A general schematic is provided in Figure 9 and the simulations were initiated in the same manner as the 1D simulations, with a high speed flow impinging upon a wall, resulting in a shock propagating in the opposite direction. The difference being, however, that the 2D simulations required an initial perturbation to initiate disturbances in the transverse direction. While such disturbances can have any number of origins in an actual shock tube¹⁴, they are explicitly included in the numerical experiment as small perturbations in order to accelerate the growth of instabilities and make the numerical simulations tractable. Such perturbations must be sufficiently random and weak as to not overshadow

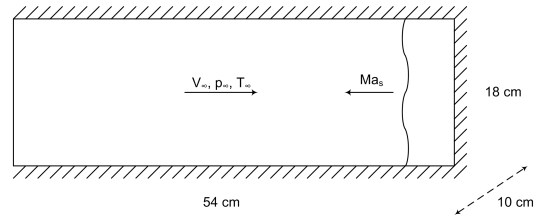


FIG. 9. Numerical setup for 2D unsteady shock tube simulations.

the dynamics inherent in the model, yet strong enough to initiate pressure disturbances that can essentially be amplified by the true dynamics.

Simulations have been performed for two of the cases, Mach 16.5 and 14.7. All simulations shown were run on a Cartesian mesh with $\Delta x = \Delta y = 0.33$ mm and have taken into account excited levels only from the 4s manifold of neutral argon. Although it was shown in the 1D simulations that higher levels are required to obtain good agreement in the radiative cooling region, the induction zone was for the most part unaffected. Therefore, neglecting the levels beyond those contained in the 4s manifold should have negligible effect on the overall dynamics of the instability in the induction zone, which is the primary interest here, while significantly accelerating the computations.

B. Mach 16.5 case

Figure 10 shows the evolution of the Mach 16.5 ionizing shock from a nearly planar wave to a self-sustaining oscillating pattern. Contours of the computed refractive index are shown, especially useful to visualize the density gradients with a high level of contrast. The initial perturbation, visible as a half-sine wave bulge in the shock front, generates transverse waves that are apparently random in nature. After propagating a few centimeters, however, the waves begin to oscillate with a resonant frequency, creating the strong incident and reflected shock pattern that is clearly visible.

Figure 11 provides snapshots of the same simulation at a later time as generated by two different visualization techniques. The top figure shows a finite-fringe interferogram generated from the numerical simulations; this clearly shows the corrugations in the shock front and an overall pattern similar to the UTIAS experiments. The refractive index plot below, taken at a later time, further reveals a well-defined structure behind the shock, having a periodic nature in the transverse direction, and strong vorticity generated within the shock region. From an investigation of the wave structure it was determined that the shock front actually consists of incident and reflected shocks as well as Mach stems, the intersection of which forms a series of triple points. These nodes appear in a quite regular pattern in both the longitudinal and transverse directions, indicating a resonant phenomenon.

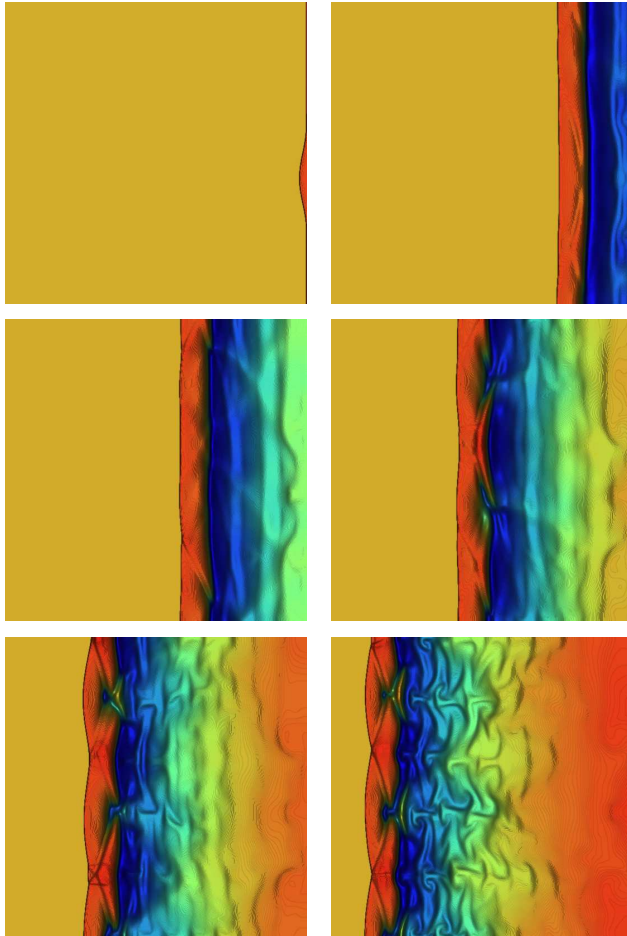


FIG. 10. Evolution of shock structure for Ma 16.5. Contours of refractive index.

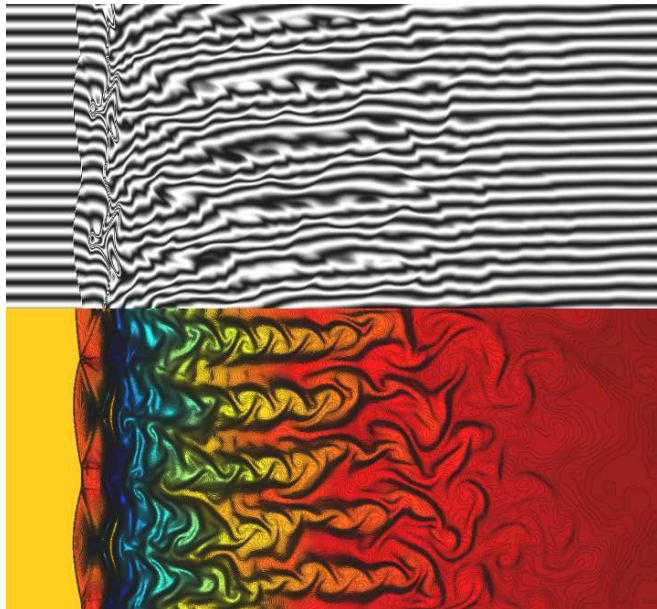


FIG. 11. Simulated interferogram and refractive index for 2D Mach 16.5 shock. The shock front consists of incident and reflected shock waves. Colormap: *min* *max*

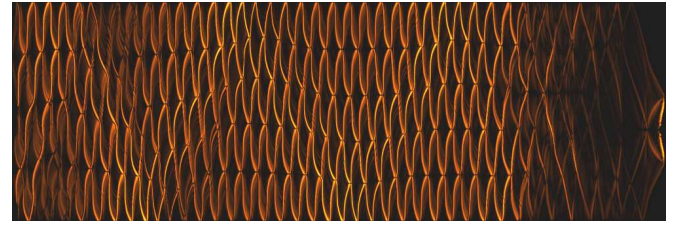


FIG. 12. Trace of triple points for Mach 16.5 case exposing ionizing cell structure. Brighter regions correspond to stronger flow vorticity.

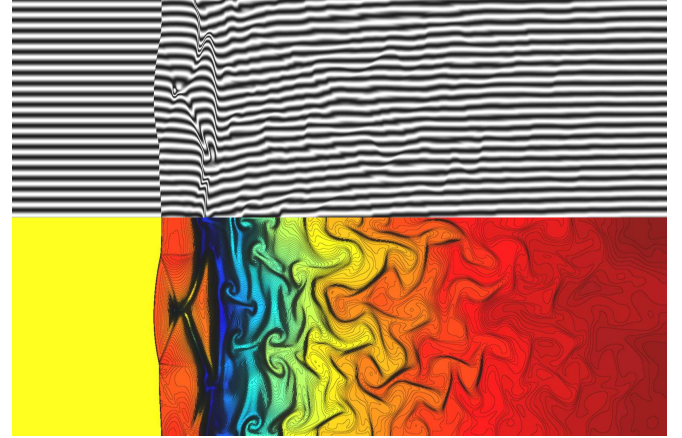


FIG. 13. Simulated interferogram and refractive index for 2D Mach 14.7 shock. Colormap: *min* *max*

These triple points are the source of the vorticity observed as far downstream as 10-15 times the induction length. The trace of these triple points, given in Figure 12, highlights a cellular structure remarkably similar to detonation cells. These analogous *ionization* cells initiate at the intersection of two triple points, which are not only the source of maximum vorticity, but also of maximum temperature and ionization; they can be thought as the two-dimensional analog to the one-dimensional electron avalanche. The resulting pressure wave generated by the increase in electron number density at this point travels radially outward, as indicated by the trace of triple points. Figure 12 can be considered the equivalent of a soot trace commonly used in experimental studies of gaseous detonations.

C. Mach 14.7 case

The case of a Mach 14.7 shock was also simulated, and from the snapshots in Figure 13, as well as the simulated soot trace in Figure 14, it is clear that decreasing the Mach number has increased the cell size in both the longitudinal and transverse directions. A direct comparison of the experimental and simulated results for the Mach 14.7 case is presented in Figure 15. As it can be seen, the shock structure is well-predicted by the numerical

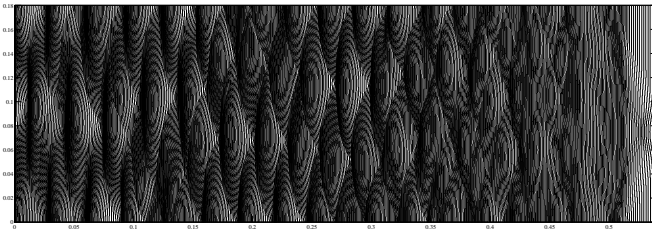


FIG. 14. Numerical soot trace for Mach 14.7 case, exposing ionizing cell structure. Image was made by super-imposing instantaneous snapshots of the shock front.

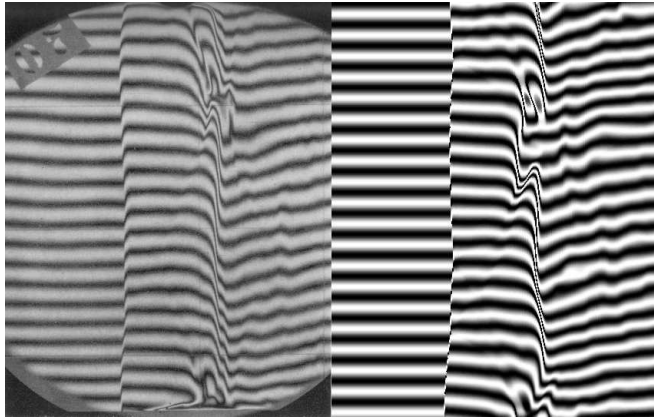


FIG. 15. Direct comparison of experimental and numerical results for Mach 14.7 shock. Clearly evident are the corrugations in the compression shock as well as unique formation patterns in the electron avalanche which are accurately reproduced by the solver.

simulations, with similar relaxation lengths and discontinuous gradients in the electron avalanche region along the transverse direction. The agreement is sufficiently close that a similar shock structure can be overlaid upon on the experimental results showing excellent agreement and compatibility with the visible structures. In particular, the pattern of incident and reflected shocks is clear in the fringe shifts of the interferogram.

D. Cellular structure

Estimation of the 2D cell size was provided in⁵, using the 1D periodicity calculation and assuming that the longitudinal periodicity must equal the transverse wave propagation time across the height (y -dir) of one complete cell. The cell width could therefore be estimated by

$$\delta \approx (a_2 + v_2 \tau)^0, \quad (18)$$

where the bulk velocity in the transverse direction behind the shock, v_2 , is assumed to be zero, and δ corresponds to a half-wavelength of the shock curvature observed in the UTIAS experiments. Using the periodicity as determined

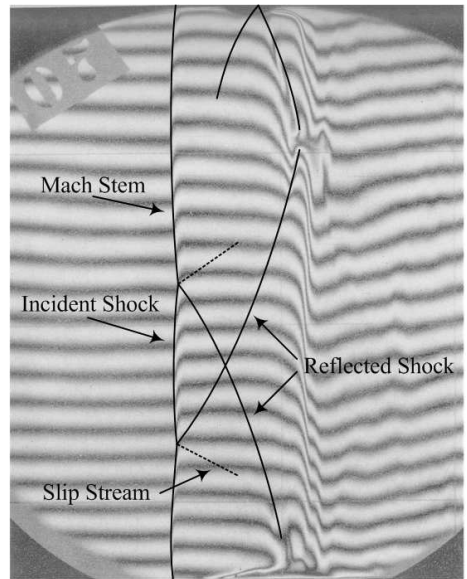


FIG. 16. Details of the 2D ionizing shock structure for the Mach 14.7 case.

in the 1D Mach 15.9 simulations as a reference case, the periodicity of the Mach 14.7 and 16.5 cases can roughly be approximated by

$$\tau' \simeq \frac{Ma}{Ma'} \frac{\ell'}{\ell} \tau. \quad (19)$$

From this it is found $\tau'_{Ma14.7} \simeq 77 \mu\text{sec}$ and $\tau'_{Ma16.5} \simeq 28 \mu\text{sec}$. Inserting these values into Eq. 18 gives $\delta_{Ma14.7} \simeq (2658 \text{ m/s})(77 \mu\text{sec}) \simeq 20 \text{ cm}$ and $\delta_{Ma16.5} \simeq (2973 \text{ m/s})(28 \mu\text{sec}) \simeq 8.3 \text{ cm}$. The predicted cell height for the Mach 16.5 case agrees favorably with the numerically-observed value of 7.2 cm, while the Mach 14.7 case is somewhat over-predicted, with a maximum observed value of just under 14 cm. However, this case is the most sensitive to finite-size effects of the shock tube; as we expect boundary-layer effects to shorten the effective induction length, the transverse size of the ionization cell would be also affected. Notwithstanding these boundary-layer effects, we can claim a good agreement over the range of Mach number studied.

The experimental shock structure can be inferred from the simulated interferogram. In IV D, we trace the incident and reflected shocks matching the shift in fringes in the induction zone.

In a similar fashion, Buchanan¹⁵ drew schematics of the Schlieren images, reproduced here in Fig. 17. These also indicate the ionization cell structure and its size. It is of course more difficult to manually extract this information from Schlieren pictures than from numerical simulations. Nevertheless, Buchanan was able to deduce a trend for the correlation between the number of observed half-wavelengths (cell size), the equilibrium values of the electron number density (n_e^*) and the shock Mach number (M_s). Buchanan postulated that the energy transfer rate between electrons and heavy particles

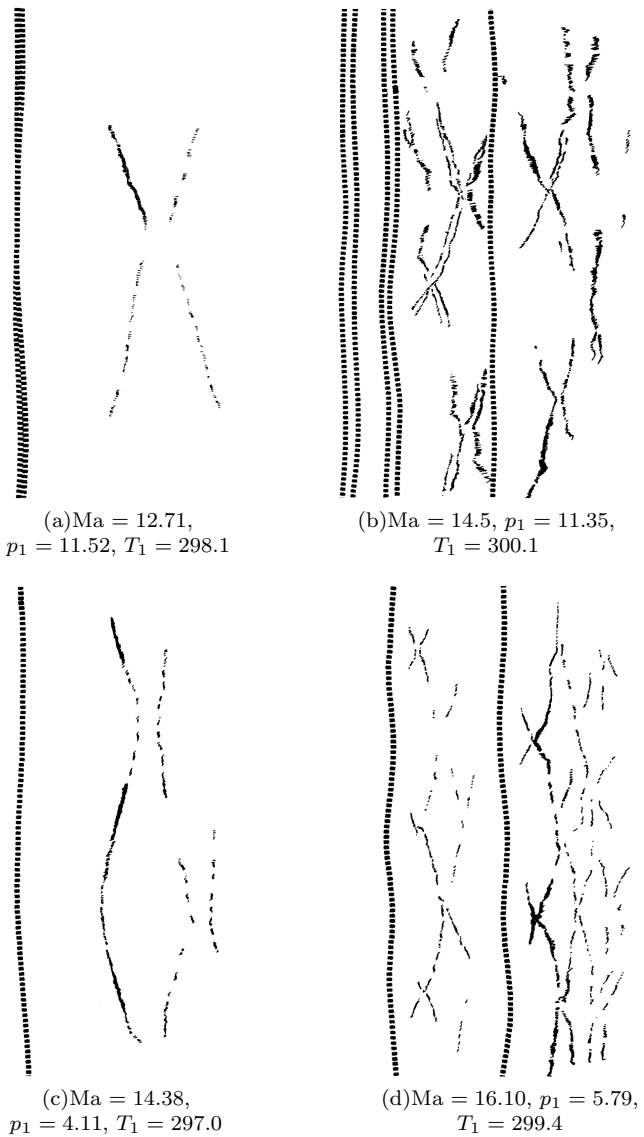


FIG. 17. Schematics of experimental Schlieren images obtained by Buchanan¹⁵. The shock structure to the right of the translational shock front (thick dotted line) clearly show the structure of the ionization cells. The number of half-cells per shocktube channel width is 2, 5, 3, and 6 for cases (a)–(d) respectively.

played a role in the oscillations, citing the work of Morse and Ingard¹⁶, and used $T_h - T_e$, n_e , n_h as indicators. As was shown in Part 1 with steady-state calculations, this role is played by the ladder-climbing mechanism, and T_e is only an approximate indication of the status of the Atomic State Distribution Function (ASDF), which is characterized by two sets of temperatures, describing the deviations from Boltzmann and Saha equilibrium. Thus, the picture is somewhat more complex than Buchanan envisioned. Nevertheless, it would be worthwhile at some point in the future to pursue a systematic study of all cases considered by Buchanan and compare the results.

V. CONCLUSIONS

Following Part 1 of this article where a detailed collisional-radiative model of argon was described and tested against structures of ionizing shocks in argon, we extended the computations to account for unsteady and multi-dimensional effects. We found that the structure of density profiles within the induction zone can be very easily explained by a periodic wave propagation between the avalanche region and the shock front. Fluctuations in electron pressure (and therefore total pressure) emanate from the avalanche region, subject to very rapid changes in electron kinetics and propagate towards the shock, where they are reflected. The shock is accelerated and the reflected contact wave separates a region of higher temperature and faster kinetics, leading to a new fluctuation in the location of the ionization avalanche. When multi-dimensional effects are considered, this process invites the formation of transverse waves, and a cellular structure is clearly observed. This pattern matches experimental observations fairly well, accounting for limitations in both the numerical model (no boundary layer, 2D only) and the experiments. This formerly conjectured⁵ dynamical effect has now been convincingly demonstrated here, as well as the analogy with cellular structures in gaseous detonations, as evidenced for example by the numerical soot trace patterns. Thus, the observation of such structures in non-equilibrium shock dynamics does not have to rely on the exo-thermicity of chemical reactions, but on the presence of a significant induction zone followed by a narrow avalanche region characterized by very rapid, non-linear chemical kinetics, and thus extremely sensitive to fluctuations in the conditions within the induction zone. The ladder-climbing process of a noble gas ASDF provides such conditions.

There is clearly a lot that can be learned from shock-tube studies, and we have shown that for argon, the unsteady phenomena, if properly visualized, can provide a wealth of information to better validate the chemical (collisional-radiative) models. This also implies that the corresponding numerical models must be able to accurately reproduce these unsteady and multi-dimensional effects. As shown here, this capability is within reach. Although we have limited the level of detail of the CR model for the multi-dimensional studies, we have a strong confidence that the detailed model can be applied in 2D and even 3D simulations on reasonably-sized computing platforms. We are currently working towards improving the efficiency of the computational approach, and since most of the computational cost lies in the CR kinetics, higher dimensionality or addition of the Navier-Stokes terms does not present undue challenges. Thus, future work will aim at more complete and more detailed capabilities in those directions; combined with state-of-the-art visualization and diagnostic techniques with high time and spatial resolution, such numerical capabilities will prove valuable for the study of non-equilibrium high-

temperature gas dynamics in modern shock-tube experiments.

ACKNOWLEDGMENTS

We wish to acknowledge the support of the Air Force Office of Scientific Research (AFOSR), grant No. 02PR05COR (PM: Dr. F. Fahroo) for this work.

VI. REFERENCES

- ¹I. I. Glass and W. S. Liu, "Effects of hydrogen impurities on shock structure and stability in ionizing monatomic gases. Part 1. Argon," *J. Fluid Mech.*, **84**, 55 (1978).
- ²M. P. F. Bristow and I. I. Glass, "Polarizability of singly ionized argon," *Phys. of Fluid*, **15**, 2066 (1972).
- ³P. I. Brimelow, "An interferometric investigation of shock structure and its induced shock-tube boundary layer in ionized argon," *Tech. Rep. 187* (UTIAS, 1974).
- ⁴A. F. P. Houwing, T. J. McIntyre, P. A. Taloni, and R. J. Sandeman, "On the population of the metastable states behind unstable shock waves in ionizing argon," *J. Fluid. Mech.*, **170**, 319 (1986).
- ⁵J.-L. Cambier, "Numerical simulations of a nonequilibrium argon plasma in a shock-tube experiment," in *Proceedings of the 22nd Fluid Dynamics, Plasma Dynamics, and Lasers Conference* (AIAA, Honolulu, HI, 1991) pp. 1–20.
- ⁶S. Brassier and G. Gallice, "A Roe scheme for the bi-temperature model of magnetohydrodynamics," *Computers and Mathematics with Applications*, **41**, 257 (1998).
- ⁷B. Einfeldt, C. Munz, P. Roe, and B. Sjogreen, "On Godunov-type methods near low densities," *J. Comput. Phys.*, **92**, 273 (1991).
- ⁸B. van Leer, "Towards the ultimate conservative difference scheme. IV. A new numerical approach to numerical convection," *J. Comput. Phys.*, **23**, 276 (1977).
- ⁹A. Suresh and H. T. Huynh, "Accurate monotonicity-preserving schemes with Runge-Kutta time stepping," *J. Comput. Phys.*, **136**, 83 (1997).
- ¹⁰W. Fickett and W. C. Davis, *Detonation*, 1st ed. (University of California Press, Berkeley, 1972).
- ¹¹R. L. Alpert and T. Y. Toong, "Periodicity in exothermic hypersonic flows about blunt projectiles," *Acta Astronautica*, **17**, 538 (1972).
- ¹²E. S. Oran and J. P. Boris, *Numerical Simulation of Reactive Flow*, 1st ed. (Elsevier Science Publishing Co., Inc., New York, 1987) ISBN 0-444-01251-6.
- ¹³The actual width of the UTIAS shock tube was 17.78 cm with a depth of 10.16 cm².
- ¹⁴Including turbulence, boundary layer effects, wall irregularities, etc.
- ¹⁵W. L. Buchanan, "An experimental study of nonstationary instabilities of planar shock waves in ionizing argon," *Tech. Rep. 222* (UTIAS, 1980).
- ¹⁶P. M. Morse and K. U. Ingard, *Theoretical Acoustics*, 1st ed. (McGraw-Hill Book Company, New-York, 1968).

Appendix A: Pressure derivatives

In the following, we define an average adiabatic index:

$$\gamma_h - 1 \equiv \frac{\sum_{s \neq e} \rho_s (k_B/m_s)}{\sum_{s \neq e} \rho_s c_{v,s}} \quad (\text{A1})$$

where s is the species index, m_s its molecular mass and $c_{v,s}$ the constant-volume specific heat (per unit mass) of that species. The total pressure derivatives, which enter in the definition of the flux jacobian, are:

$$P_E \equiv \left(\frac{\partial p}{\partial E} \right)_{q \neq E} = \gamma_h - 1 \quad (\text{A2})$$

$$P_{S_e} \equiv \left(\frac{\partial p}{\partial S_e} \right)_{q \neq S_e} = \rho^{\gamma_e - 1} \left(1 - \frac{\gamma_h - 1}{\gamma_e - 1} \right) \quad (\text{A3})$$

$$P_{\vec{m}} \equiv \left(\frac{\partial p}{\partial \vec{m}} \right)_{q \neq \vec{m}} = -(\gamma_h - 1) \vec{u} \quad (\text{A4})$$

$$P_{\rho_e} \equiv \left(\frac{\partial p}{\partial \rho_e} \right)_{q \neq \rho_e} = (\gamma_e - \gamma_h) \frac{p_e}{\rho} + (\gamma_h - 1) \frac{\vec{u}^2}{2} \quad (\text{A5})$$

$$P_{\rho_{s \neq e}} \equiv \left(\frac{\partial p}{\partial \rho_{s \neq e}} \right)_{q \neq \rho_{s \neq e}} = P_{\rho_e} - (\gamma_h - 1) \varepsilon_s + \frac{p_s}{\rho_s} \quad (\text{A6})$$

$$P_\rho \equiv \left(\frac{\partial p}{\partial \rho} \right)_{q \neq \rho} = \sum_s y_s P_{\rho_s} = P_{\rho_e} - (\gamma_h - 1) \sum_{s \neq e} y_s \varepsilon_s + \frac{p - p_e}{\rho} \quad (\text{A7})$$

where $y_s = \rho_s / \rho$.

$$P_{eS_e} \equiv \left(\frac{\partial p_e}{\partial S_e} \right)_{q \neq S_e} = \rho^{\gamma_e - 1} = \frac{p_e}{S_e} \quad (\text{A8})$$

$$P_{e\rho_s} \equiv \left(\frac{\partial p_e}{\partial \rho_s} \right)_{q \neq \rho_s} = (\gamma_e - 1) \frac{p_e}{\rho} \quad (\text{A9})$$

$$P_{e\rho} \equiv \left(\frac{\partial p_e}{\partial \rho} \right)_{q \neq \rho} = P_{e\rho_s} \quad (\text{A10})$$